



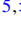



Modification of interfacial spin-orbit torque in Co/Pt/oxide hybrid structuresTakamasa Hirai ^{1,2,3,*}, Kento Hasegawa ^{1,2}, Shinya Ota,^{1,2} Motohiro Suzuki ^{4,†},
Tomohiro Koyama ^{2,5} and Daichi Chiba ^{2,5,‡}¹*Department of Applied Physics, The University of Tokyo, Bunkyo, Tokyo 113-8656, Japan*²*The Institute of Scientific and Industrial Research (SANKEN), Osaka University, Ibaraki, Osaka 567-0047, Japan*³*National Institute for Materials Science, Tsukuba, Ibaraki 305-0047, Japan*⁴*Japan Synchrotron Radiation Research Institute, Sayo, Hyogo 679-5198, Japan*⁵*Center for Spintronics Research Network at Osaka University, Toyonaka, Osaka 560-6671, Japan* (Received 28 April 2021; revised 24 August 2021; accepted 8 September 2021; published 1 October 2021)

We investigate current-induced spin-orbit torque (SOT) in Co/Pt/oxide systems by varying a sort of the oxide layer. When the Pt thickness is less than ~ 2 nm, Pt at the interface of the oxide layer is magnetically polarized owing to the magnetic proximity effect. In these systems, fieldlike (FL) SOT depends significantly on the adjacent oxide material, whereas dampinglike SOT is almost irrelevant to oxides. The FL SOT efficiency of the Pt/HfO₂ sample is 2.2 times greater than that of the Pt/MgO sample at the maximum. X-ray magnetic circular dichroism spectroscopy reveals that the anisotropy of the Pt orbital magnetic moment varies with the oxide material, suggesting that the modulation of the electronic structure at the Pt/oxide interface contributes to SOT enhancement.

DOI: [10.1103/PhysRevB.104.134401](https://doi.org/10.1103/PhysRevB.104.134401)**I. INTRODUCTION**

In the field of spintronics, tailoring a thin-film stack affords a variety of fascinating static and transport magnetic phenomena via spin-orbit coupling (SOC) [1–4]. Recently, one SOC-driven phenomenon, current-induced spin-orbit torque (SOT), which appears in a ferromagnet (FM)/heavy metal (HM) layered structure, has attracted much attention as a promising technology for high-speed information writing. To clarify the underlying mechanisms, many researches of SOT have been intensively addressed in various layer structures based on FM/HM systems [5–9]. In addition, previous studies have reported that the oxide capping layer on the FM layer imposes a nontrivial effect on both fieldlike (FL) and dampinglike (DL) SOTs [8,10]. The SOT modulation is assumed to be induced by an electronic mechanism, such as the modification of the interfacial Rashba-Edelstein effect (REE) at the FM/oxide interface [10,11]. However, some reports indicate that in similar structures, the chemical (e.g., the oxidation of the FM layer and/or FM interface) or structural (e.g., the crystallinity and magnetic dead layer) factors also affect SOT [8,10,12–16]. Hence, it is difficult to elucidate the origin of changes in SOT.

In this paper, we report the study of SOT in Ta/Co/Pt/oxide films by changing the adjacent oxide material, where the magnetic moment is induced into the HM Pt layer from the Co layer. Owing to the high ionization energy of Pt, the difference

in chemical and structural properties by the deposition of different oxide materials is almost negligible; thus, solely the effect of electronic structure modulation can be investigated. In the system with less than 2.0-nm-thick Pt layer, FL SOT is sensitive to the oxide type, whereas DL SOT does not depend significantly on the oxide in all Pt/oxide samples. In addition, an investigation of the magnetic anisotropy and the spin and orbital magnetic moments in Pt using the synchrotron x-ray magnetic circular dichroism (XMCD) measurements indicates the difference in the electronic structure of Pt-5*d* orbitals regarding oxides. Our results suggest that SOT that emerges at the interface of polarized Pt/oxide can be modified considerably through engineering the interfacial electronic state between the Pt and oxide layers.

II. SAMPLE PREPARATION

The layer structures used in the SOT study are illustrated in Fig. 1(a). A metal trilayer, comprising Ta(1.6 nm)/Co(3.2 nm)/Pt(*t*_{Pt}), was deposited on a thermally oxidized Si substrate by rf magnetron sputtering at room temperature. Here, several samples with different *t*_{Pt} values (=0.74–3.0 nm) were prepared. After the deposition, the samples were removed from the sputtering chamber to the air and divided into some pieces. Subsequently, three types of oxide layers, HfO₂(5.0 nm), Al₂O₃(5.0 nm), and MgO(1.5 nm)/HfO₂(5.0 nm) layer were grown on each film (denoted as “Pt/HfO₂,” “Pt/Al₂O₃,” and “Pt/MgO” hereinafter, respectively), where rf magnetron sputtering was used to deposit MgO, and atomic layer deposition (ALD) to deposit HfO₂ and Al₂O₃. In the sputtering (ALD) process, the oxide layer was grown in the Ar-filled (N₂-filled) chamber at room temperature (150 °C). Although the top Pt layer protects the sample from natural oxidation, the samples

*HIRAI.Takamasa@nims.go.jp

†Present address: Kwansai Gakuin University, Sanda, Hyogo 669-1337, Japan.

‡dchiba@sanken.osaka-u.ac.jp

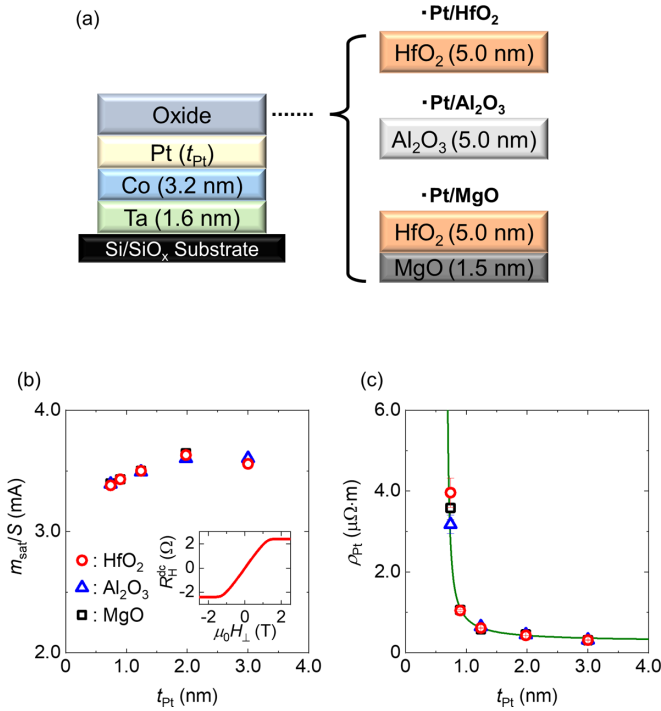


FIG. 1. (a) Cross-sectional view of layer structures used for SOT experiments. (b) Pt thickness dependence of areal saturation magnetic moment. Inset shows dc Hall resistance measured by sweeping perpendicular magnetic field for Pt(0.74 nm)/HfO₂ sample. (c) Pt thickness dependence of Pt resistivity. Solid line shows resistivity calculation [27].

before covering the oxide layer were kept in the load lock chamber of the sputtering machine during the deposition of each oxide layer. For comparison of SOT, we also prepared the sample with the bare Pt surface of $t_{\text{Pt}} = 0.74$ and 3.0 nm. To align baking time, all the samples were annealed in an ALD chamber for 2 h at 150 °C under N₂ atmosphere. The samples were processed into a wire structure with 15- μm width w using photolithography and Ar ion milling. Finally, electrodes with Cr(3 nm)/Cu(60 nm)/Au(10 nm) contact pads were formed at the end of the Hall bar using lift-off method.

III. EXPERIMENTAL RESULTS

A. Magnetization and Pt resistivity measurements

The inset of Fig. 1(b) shows the out-of-plane magnetic field H_{\perp} dependence of the dc Hall resistance R_{H}^{dc} for the Pt/HfO₂ sample with $t_{\text{Pt}} = 0.74$ nm, indicating that the easy axis is in the in-plane direction. It was also confirmed that all the SOT devices have the in-plane magnetization easy axis. Figure 1(b) shows the dependence of the saturation magnetic moment per unit area m_{sat}/S at 300 K on t_{Pt} for each sample. In all the Pt/oxide samples, m_{sat}/S increases with t_{Pt} up to 2 nm, but no significant increase in m_{sat}/S is observed at $t_{\text{Pt}} = 3.0$ nm, which is attributed to the well-known magnetic proximity effect (MPE) in Pt. In a FM/HM bilayer [17–22], the FM layer induces a magnetic moment in the neighboring HM layer through the hybridization of each d orbital. The MPE decays from the FM/HM interface, indicating that the magnetic moment at the Co/Pt interface is larger than that at the

Pt/oxide interface. The MPE length obtained here (~ 2 nm) is consistent with those reported in previous studies [17,19]. The current shunting of the multilayer was estimated by measuring the sheet resistances of the Pt/oxide samples, Ta(1.6 nm)/MgO sample, and Ta(1.6 nm)/Co(3.2 nm)/MgO sample using a standard four-probe method. The t_{Pt} dependence of the Pt resistivity ρ_{Pt} is shown in Fig. 1(c). The significant increase in ρ_{Pt} with decreasing t_{Pt} is due to the interface and/or grain-boundary scattering [23], which is consistent with previous reports regarding continuous ultrathin Pt films [24–27]. Note that the magnitudes of ρ_{Pt} among three Pt(0.74 nm)/oxides are slightly different among three Pt(0.74 nm)/oxide samples, but even assuming this difference is completely originating from the difference in t_{Pt} , such as the thickness of dead layer due to the difference in the deposition methods, it is calculated to be at most ~ 0.005 nm, which is much smaller than the atomic radius of Pt; thus, the difference in t_{Pt} in our Pt/oxide samples is considered to be ignorable. The values of both m_{sat}/S and t_{Pt} are similar in the three Pt/oxide samples, implying that the crystal structure and effective thickness of polarized Pt are independent of the neighboring oxide material.

B. Spin-orbit torque measurement

For the quantitative determination of DL and FL SOTs, harmonic Hall measurements were performed at 300 K [16,28,29]. We characterized the DL and FL SOT effective-field vectors as $\mathbf{H}_{\text{DL}} = H_{\text{DL}}(\hat{\mathbf{M}} \times \hat{\mathbf{y}})$ and $\mathbf{H}_{\text{FL}} = H_{\text{FL}}[\hat{\mathbf{M}} \times (\hat{\mathbf{y}} \times \hat{\mathbf{M}})]$. Here $\hat{\mathbf{M}}$ and $\hat{\mathbf{y}}$ are the unit vectors along the magnetization and y axis [see Fig. 2(a)], respectively, and $H_{\text{DL(FL)}}$ is the proportionality constant of the DL (FL) SOT effective field. An ac charge current $I \sin \omega t$ with frequency $\omega/2\pi = 13.14$ Hz was injected along the x axis. We defined $+I$ as current flowing along the $+x$ direction. The in-phase first harmonic voltage (V_{H}^{ω}) and the out-of-phase second-harmonic voltage ($V_{\text{H}}^{2\omega}$) were measured using a lock-in amplifier with rotating in-plane external magnetic field H from $\varphi = 0^{\circ}$ to 360° with respect to the $+x$ direction. When the sample magnetization \mathbf{M} is uniformly aligned along the in-plane H direction, the first and second-harmonic Hall resistances ($R_{\text{H}}^{\omega} = V_{\text{H}}^{\omega}/I$ and $R_{\text{H}}^{2\omega} = V_{\text{H}}^{2\omega}/I$, respectively) are simply expressed as

$$R_{\text{H}}^{\omega} = R_{\text{P}} \sin 2\varphi, \quad (1)$$

$$R_{\text{H}}^{2\omega} = -R_{\text{FL}}(\cos 3\varphi + \cos \varphi) - (R_{\text{DL}} + R_{\text{T}}) \cos \varphi, \quad (2)$$

where R_{P} , R_{FL} , R_{DL} , and R_{T} represent the planar Hall resistance, FL (including the Oersted field), DL, and field-independent thermal Hall resistance associated with the anomalous Nernst effect and the longitudinal spin Seebeck effect [28], respectively. The values of R_{P} , R_{FL} , and $R_{\text{DL}} + R_{\text{T}}$ were determined from the sinusoidal fitting of the measured R_{H}^{ω} and $R_{\text{H}}^{2\omega}$ [Figs. 2(b) and 2(c)] [16]. Then, we quantified H_{DL} and H_{FL} by fitting the H dependence of $R_{\text{DL}} + R_{\text{T}}$ and R_{FL} based on the following relations [16]:

$$R_{\text{DL}} = \frac{1}{2} \frac{R_{\text{A}} H_{\text{DL}}}{H + |H_{\text{k}}|}, \quad (3)$$

$$R_{\text{FL}} = \frac{1}{2} \frac{R_{\text{P}}(H_{\text{FL}} + H_{\text{Oe}})}{H}, \quad (4)$$

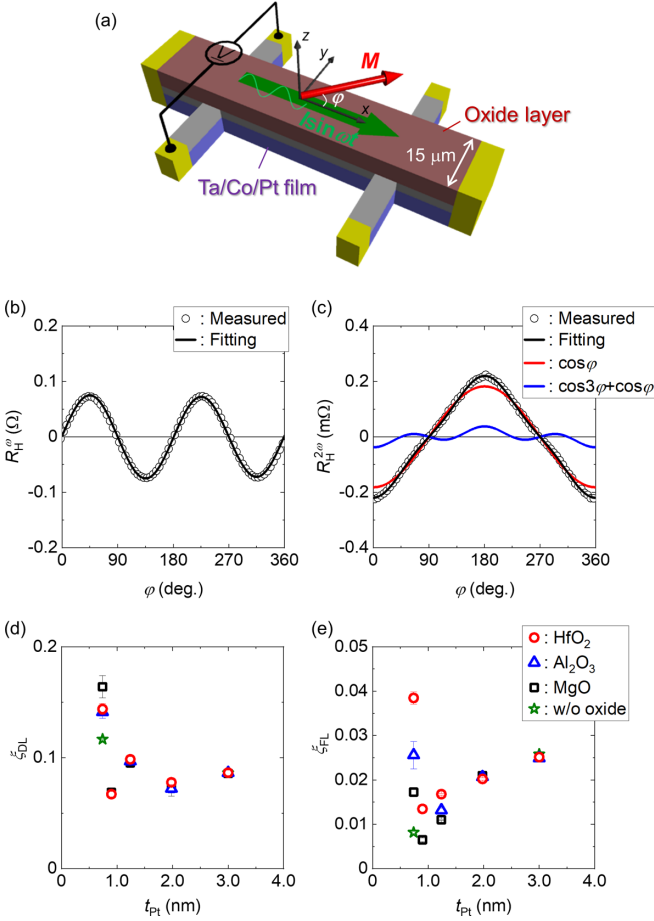


FIG. 2. (a) Schematic illustration of device structure and experimental setup for harmonic Hall measurements. (b) First harmonic and (c) second-harmonic Hall resistance in the Pt(3.0 nm)/HfO₂ sample at in-plane magnetic field of 0.3 T and ac charge current with the magnitude of 5.5 mA. Black solid lines show fitting result estimated using Eqs. (2) and (3). Red and blue solid lines in (c) show DL and FL terms, respectively. (d), (e) Pt thickness dependence of DL and FL SOT efficiencies for three Pt/oxide samples.

where R_A is the anomalous Hall resistance, H_k the anisotropy field, and H_{Oe} the Oersted field generated by the current flow in the Pt and Ta layers. The magnitudes of R_A and H_k were estimated from the R_H^{dc} versus H_{\perp} curve [30,31], and H_{Oe} was calculated using the simplified Ampère law: $(I_{Pt} - I_{Ta})/2w$, where I_{Pt} and I_{Ta} , respectively, denote the current flow in the Pt and Ta layer. Finally, we calculated the DL and FL SOT efficiencies per unit current density (ξ_{DL} and ξ_{FL} , respectively) of each sample, which is a benchmark for evaluating the performance of the SOT generation, using the following equation:

$$\xi_{FL(DL)} = \frac{2e}{\hbar j} \frac{\mu_0 m_{sat} H_{FL(DL)}}{S}, \quad (5)$$

with e , \hbar , and j being the elementary charge, reduced Planck's constant, and current density in the HM layers, respectively. The t_{Pt} dependence of ξ_{DL} and ξ_{FL} of three Pt/oxide samples is summarized in Figs. 2(d) and 2(e), respectively. The signs of ξ_{DL} and ξ_{FL} are always positive for all the samples. The

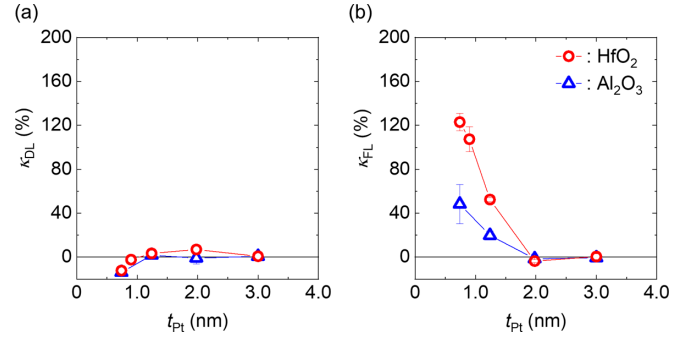


FIG. 3. [(a), (b)] Pt thickness dependence of change ratio of DL (FL) SOT efficiency for the Pt/HfO₂ and Pt/Al₂O₃ samples.

t_{Pt} dependences of ξ_{DL} and ξ_{FL} in each Pt/oxide sample differ from those previously obtained for HM/Pt/FM trilayer or Pt/FM bilayer systems [25,32,33], but are qualitatively similar to the theoretical calculation taking both the bulk spin-Hall effect (SHE) and the interfacial REE into consideration [34]. Then, we focus on the adjacent oxide dependence of SOT. ξ_{DL} exhibits the minimal correlation with the adjacent oxide material over the entire range of t_{Pt} . On the other hand, the plot of ξ_{FL} versus t_{Pt} presents the peculiar oxide dependence. First, below t_{Pt} of about 1.3 nm, the Pt/HfO₂ sample indicates the largest ξ_{FL} value, and the Pt/Al₂O₃ and Pt/MgO samples follow in descending order. Then, the difference in ξ_{FL} becomes negligible for the sample with $t_{Pt} = 2.0$ and 3.0 nm. In Figs. 2(d) and 2(e), ξ_{DL} and ξ_{FL} for the Pt(0.74 and 3.0 nm) without oxide layers on top are also shown. Slightly (a great deal) smaller ξ_{DL} (ξ_{FL}) than that in the Pt/HfO₂ sample is obtained at $t_{Pt} = 0.74$ nm, whereas the magnitudes of both ξ_{DL} and ξ_{FL} are the same as those in the sample with oxide layers at $t_{Pt} = 3.0$ nm. These tendencies are quite different from the cases with the modulation of an oxidation or composition state in the Co/Pt system [12–14]. Next, we estimated the change ratio of $\xi_{DL(FL)}$, which is defined as $\kappa_{DL(FL)}^{H(A)} = (\xi_{DL(FL)}^{H(A)} - \xi_{DL(FL)}^M) / \xi_{DL(FL)}^M$, where $\xi_{DL(FL)}^{H(A)}$, $\xi_{DL(FL)}^A$, and $\xi_{DL(FL)}^M$ are $\xi_{DL(FL)}$ for Pt/HfO₂, Pt/Al₂O₃, and Pt/MgO, respectively. Figures 3(a) and 3(b) show the t_{Pt} dependences of $\kappa_{DL}^{H(A)}$ and $\kappa_{FL}^{H(A)}$. The monotonic reduction of $\kappa_{FL}^{H(A)}$ with increasing t_{Pt} up to ~ 2 nm is observed, whereas t_{Pt} dependence of κ_{DL} is very small.

Then, we consider interpreting the results of our SOT measurements in the Pt/oxide hybrid systems. First, as each layer thickness and resistivity are the same among the three Pt/oxide samples, SOT originating from the SHE in Pt (even though the magnetic moment is fully induced in the Pt layer [35]) and Ta layers is unaffected by the adjacent oxide material. Similarly, the spin transparency across the Co/Pt interface is expected to remain unchanged. These might reflect oxide-independent DL SOT shown in our measurements [15,34,36]. Hereafter, we focus on the contribution of REE-mediated SOTs. In general, the REE exerts SOT via two scenarios: the exchange coupling at a ferromagnetic interface and the spin-transfer effect by diffusive spin-current generation [34]. In the previous report pertaining to the Pt/Co system, the modulation of the latter contribution only affects the change in DL SOT [37]; however,

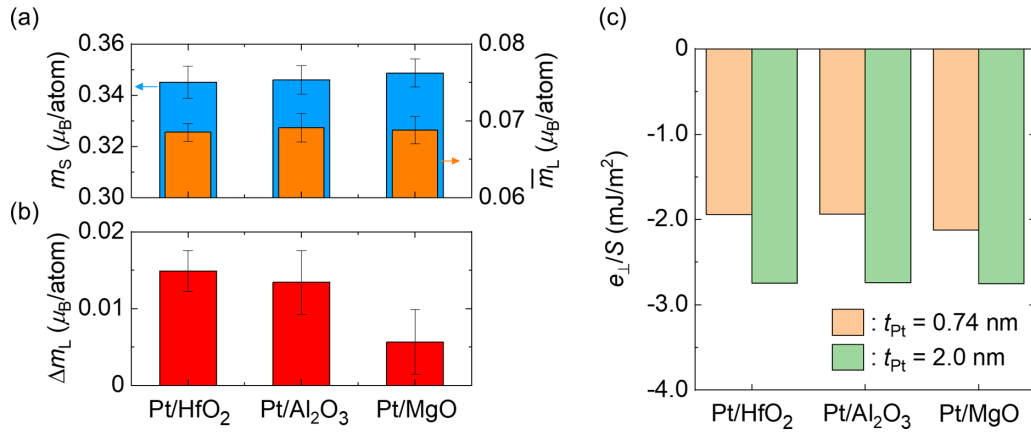


FIG. 4. (a) Spin magnetic moment m_s and average of out-of-plane (m_L^{\perp}) and in-plane (m_L^{\parallel}) components of orbital magnetic moment $\bar{m}_L = (m_L^{\perp} + m_L^{\parallel})/2$; (b) anisotropy of orbital magnetic moment $\Delta m_L = m_L^{\perp} - m_L^{\parallel}$ for three Pt(0.74 nm)/oxide samples. (c) Areal PMA energy for Pt(0.74 and 2.0 nm) with different oxide capping layer.

this effect is not observed in our case. The oxide dependence of FL SOT observed in this study gets vanishingly small towards $t_{\text{Pt}} \sim 2$ nm, which is consistent with the MPE decay length in the Pt/Co system [17,19]. Hence, our results suggest the following: (i) FL SOT is closely associated with the Pt magnetic moment at the Pt/oxide interface, and (ii) such SOT might depend on the interface character of the Pt and oxide layers.

C. X-ray magnetic circular dichroism spectroscopy of Pt

For a better understanding of the electronic state of the magnetically-polarized Pt, we performed XMCD spectroscopy at the Pt- L edges. The angle-dependent XMCD is a powerful tool for elucidating the element-specific electronic states and quantifying the spin magnetic moment (m_s) and out-of-plane (in-plane) orbital magnetic moment (m_L^{\perp} (m_L^{\parallel})) by applying the magneto-optical sum rules [27,38–42]. Figure 4(a) shows m_s for the Pt/HfO₂, Pt/Al₂O₃, and Pt/MgO samples with $t_{\text{Pt}} = 0.74$ nm. The layer structure used in the XMCD study differs slightly from that used in the SOT measurement [27]. There is no significant difference in m_s among the three samples, which is consistent with the magnetization measurement. Although the average value of m_L^{\perp} and m_L^{\parallel} , $\bar{m}_L = (m_L^{\perp} + m_L^{\parallel})/2$, is also irrelevant to the oxide layer [Fig. 4(a)], the anisotropy of the orbital magnetic moment, $\Delta m_L = m_L^{\perp} - m_L^{\parallel}$, in the Pt/MgO sample is smaller than that in the Pt/HfO₂ and Pt/Al₂O₃ samples, as shown in Fig. 4(b). The magnitude of Δm_L is related to the anisotropy of the magnetocrystalline energy [43], and the present result suggests that the perpendicular magnetic anisotropy (PMA) is enhanced by the oxide layers of HfO₂ and Al₂O₃. In Fig. 4(c), a similar tendency is obtained in the areal PMA energy, $e_{\perp}/S = \mu_0 m_{\text{sat}} H_k / 2S$ [30,31] of the Pt(0.74 nm)/MgO sample, whereas there is no difference in e_{\perp}/S for the Pt(2.0 nm)/oxide samples, where the proximity-induced magnetic moment at the Pt/oxide interface is diluted. These results provide the strong evidence regarding the modification of the interfacial electronic state in polarized Pt by changing the oxide material.

D. X-ray diffraction measurement

To estimate the structural property, we performed the x-ray diffraction (XRD) measurements with Cu- $K\alpha$ radiation in the Pt/HfO₂ samples using the conventional θ - 2θ method. Figure 5 displays the XRD profiles for the Pt(0.74 and 3.0 nm)/HfO₂ samples, where the XRD intensity of the Pt(3.0 nm)/HfO₂ sample is resized by 1/20. The three visible peaks are shown in the range of $35^\circ < 2\theta < 45^\circ$. Foremost, since the Ta and all the oxide layers in our films have amorphous structures [19], these peaks are attributed to the contribution of the Co or Pt. The fcc(111) Pt peak is confirmed at $2\theta = 39^\circ$ – 41° in both samples, although the peak obtained in the Pt(0.74 nm)/HfO₂ sample is broad due to the very thin Pt layer. The feature at $2\theta = 44.2^\circ$ – 44.5° can correspond to the fcc(111) or hcp(0002) Co layer. The peak around $2\theta = 43^\circ$, which has almost the same (much smaller) magnitude as (than) the Pt peak in the sample with $t_{\text{Pt}} = 0.74$ nm (3.0 nm), is expected to be a Co_xPt_{1-x} alloy arising from the nominal intermixing [44]. This result suggests that the interfaces at Co/Pt and even Pt/oxide in our sputtered samples are not atomically sharp.

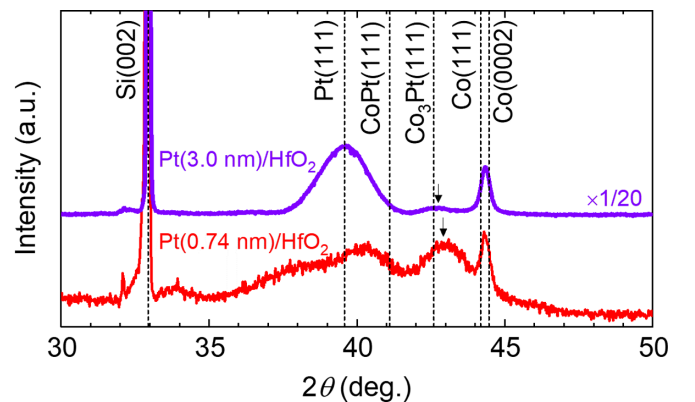


FIG. 5. XRD profiles of the Pt(0.74 and 3.0 nm)/HfO₂ samples, where the XRD intensity of the Pt(3.0 nm)/HfO₂ sample is resized by 1/20. Black arrows indicate the peaks obtained around $2\theta = 43^\circ$.

IV. DISCUSSION

Finally, we discuss the correlation between the considerable oxide dependence of FL SOT and the interfacial electronic state in the Pt/oxide system. According to the former report, the intrinsic electric dipole, which is developed at the surface of the metal layer facing the oxide layer [45], can induce an enhancement of REE-mediated SOT [11]. The strength of the interfacial dipole is dominated by the large electronegativity of the oxygen ion and its concentration. However, under the assumption that the crystallinity of the respective oxide represents the most stabilized phase, the number of oxygen atoms per unit area (n) calculated from the formula weight and density shows the relation $n(\text{Al}_2\text{O}_3) > n(\text{HfO}_2) \geq n(\text{MgO}) > n(\text{vacuum})$ [46], which cannot fully explain our experimental results: the maximum ξ_{FL} for the Pt(0.74 nm)/HfO₂ sample [Fig. 2(e)]. Another suggestion is the change in the interfacial orbital hybridization with atomic SOC, corresponding to the change in the asymmetry of the wave function near the interface atoms. The induced wave-function asymmetry can modulate the Rashba splitting [47–49]. In addition, the additional PMA induced by the REE at an asymmetric interface was predicted [50]. In our case, although it is assumed that the orbital hybridization between Pt-5d and O-2p dominantly works, the finite SOC in the Hf and Al atoms, as compared with the imperceptible SOC in the Mg atom, may cause a change in the orbital hybridization. These suggestions might be originating from pure electronic mechanisms, such as the modification of the band structure, as well as the nanoscale-structural difference at the Pt/oxide interface. Our XRD measurements imply the intermixing at the Co/Pt interface brings a greater impact on the cleanliness of the Pt/oxide interface in the thinner Pt film, which may cause the slight difference in ξ_{DL} in the Pt(0.74 nm) samples

[Fig. 2(d)]. Although our results confirm the effectiveness of the insulating oxide for the enhancement of SOT, further investigations, such as the more detailed structural analysis and SOT measurements using an epitaxially grown Pt/oxide interface, are needed to clarify the microscopic mechanism of oxide-dependent interfacial SOT.

V. SUMMARY

In summary, we have investigated current-induced SOT in the Co/Pt/oxide hybrid structures. Interfacial FL SOT is modified by engineering the interfacial electronic state of Pt/oxide. Our findings provide opportunities for material designs that will not only improve SOT in multilayer structures, but also realize the efficient active control of SOC-driven phenomena at the metal/oxide interface, such as the electric-field effect on SOTs [51,52], magnetic anisotropy [53], and chiral spin interactions [54].

ACKNOWLEDGMENTS

The authors thank A. Obinata, S. Ono, and N. Kawamura for technical support and M. Kohda and K. Uchida for useful discussions. This work was supported by Grant-in-Aid for Scientific Research (A) (Grant No. JP19H00860) and Research Fellowship for Young Scientists (Grants No. JP17J03125, No. JP18J10734, No. JP19J21938, and No. JP20J00365) from JSPS and Spintronics Research Network of Japan. Part of the work was performed using facilities at the Comprehensive Analysis Center, SANKEN and the Cryogenic Research Center, Osaka University. The x-ray spectroscopy was performed at SPring-8 BL39XU with approval from the Japan Synchrotron Radiation Research Institute (Grants No. 2018B0925 and No. 2019A0925).

-
- [1] H. Brooks, *Phys. Rev.* **58**, 909 (1940).
 [2] V. Kamberský, *Czech. J. Phys.* **26**, 1366 (1976).
 [3] N. Nagaosa and Y. Tokura, *Nat. Nanotechnol.* **8**, 899 (2013).
 [4] A. Manchon and A. Belabbes, *Solid State Phys.* **68**, 1 (2017).
 [5] I. M. Miron, K. Garello, G. Gaudin, P.-J. Zermatten, M. V. Costache, S. Auffret, S. Bandiera, B. Rodmacq, A. Schuhl, and P. Gambardella, *Nature* **476**, 189 (2011).
 [6] L. Liu, C.-F. Pai, Y. Li, H. W. Tseng, D. C. Ralph, and R. A. Buhrman, *Science* **336**, 555 (2012).
 [7] K. Garello, I. M. Miron, C. O. Avci, F. Freimuth, Y. Mokrousov, S. Blügel, S. Auffret, O. Boulle, G. Gaudin, and P. Gambardella, *Nat. Nanotechnol.* **8**, 587 (2013).
 [8] X. Qiu, K. Narayanapillai, Y. Wu, P. Deorani, D.-H. Yang, W.-S. Noh, J.-H. Park, K.-J. Lee, H.-W. Lee, and H. Yang, *Nat. Nanotechnol.* **10**, 333 (2015).
 [9] Y.-C. Lau, D. Betto, K. Rode, J. M. D. Coey, and P. Stamenov, *Nat. Nanotechnol.* **11**, 758 (2016).
 [10] M. Akyol, J. G. Alzate, G. Yu, P. Upadhyaya, K. L. Wong, A. Ekicibil, P. Khalili Amiri, and K. L. Wang, *Appl. Phys. Lett.* **106**, 032406 (2015).
 [11] S. Emori, T. Nan, A. M. Belkessam, X. Wang, A. D. Matyushov, C. J. Babroski, Y. Gao, H. Lin, and N. X. Sun, *Phys. Rev. B* **93**, 180402(R) (2016).
 [12] S. Emori, U. Bauer, S. Woo, and G. S. D. Beach, *Appl. Phys. Lett.* **105**, 222401 (2014).
 [13] Y. Hibino, T. Hirai, K. Hasegawa, T. Koyama, and D. Chiba, *Appl. Phys. Lett.* **111**, 132404 (2017).
 [14] K. Hasegawa, Y. Hibino, M. Suzuki, T. Koyama, and D. Chiba, *Phys. Rev. B* **98**, 020405(R) (2018).
 [15] H. An, S. Haku, Y. Kanno, H. Nakayama, H. Maki, J. Shi, and K. Ando, *Phys. Rev. Appl.* **9**, 064016 (2018).
 [16] T. Hirai, Y. Hibino, K. Hasegawa, M. Kohda, T. Koyama, and D. Chiba, *Appl. Phys. Express* **13**, 123005 (2020).
 [17] M. Suzuki, H. Muraoka, Y. Inaba, H. Miyagawa, N. Kawamura, T. Shimatsu, H. Maruyama, N. Ishimatsu, Y. Isohama, and Y. Sonobe, *Phys. Rev. B* **72**, 054430 (2005).
 [18] S. Y. Huang, X. Fan, D. Qu, Y. P. Chen, W. G. Wang, J. Wu, T. Y. Chen, J. Q. Xiao, and C. L. Chien, *Phys. Rev. Lett.* **109**, 107204 (2012).
 [19] T. Koyama, A. Obinata, Y. Hibino, A. Hirohata, B. Kuerbanjiang, V. K. Lazarov, and D. Chiba, *Appl. Phys. Lett.* **106**, 132409 (2015).
 [20] A. Obinata, Y. Hibino, D. Hayakawa, T. Koyama, K. Miwa, S. Ono, and D. Chiba, *Sci. Rep.* **5**, 14303 (2015).
 [21] Y. Hibino, T. Koyama, A. Obinata, K. Miwa, S. Ono, and D. Chiba, *Appl. Phys. Express* **8**, 113002 (2015).

- [22] L. J. Zhu, D. C. Ralph, and R. A. Buhrman, *Phys. Rev. B* **98**, 134406 (2018).
- [23] W. E. Bailey, S. X. Wang, and E. Y. Tsymbal, *Phys. Rev. B* **61**, 1330 (2000).
- [24] P. Fan, K. Yi, J. Shao, and Z. Fan, *J. Appl. Phys.* **95**, 2527 (2004).
- [25] M. H. Nguyen, D. C. Ralph, and R. A. Buhrman, *Phys. Rev. Lett.* **116**, 126601 (2016).
- [26] S. Dushenko, M. Hokazono, K. Nakamura, Y. Ando, T. Shinjo, and M. Shiraishi, *Nat. Commun.* **9**, 3118 (2018).
- [27] See Supplemental Material at <http://link.aps.org/supplemental/10.1103/PhysRevB.104.134401> for detailed information on the calculation of Pt resistivity and the XMCD measurement and analysis.
- [28] C. O. Avci, K. Garello, M. Gabureac, A. Ghosh, A. Fuhrer, S. F. Alvarado, and P. Gambardella, *Phys. Rev. B* **90**, 224427 (2014).
- [29] Y. C. Lau and M. Hayashi, *Jpn. J. Appl. Phys.* **56**, 0802B5 (2017).
- [30] M. Endo, S. Kanai, S. Ikeda, F. Matsukura, and H. Ohno, *Appl. Phys. Lett.* **96**, 212503 (2010).
- [31] T. Hirai, T. Koyama, A. Obinata, Y. Hibino, K. Miwa, S. Ono, M. Kohda, and D. Chiba, *Appl. Phys. Express* **9**, 063007 (2016).
- [32] H. Nakayama, K. Ando, K. Harii, T. Yoshino, R. Takahashi, Y. Kajiwara, K. Uchida, Y. Fujikawa, and E. Saitoh, *Phys. Rev. B* **85**, 144408 (2012).
- [33] A. Ganguly, K. Kondou, H. Sukegawa, S. Mitani, S. Kasai, Y. Niimi, Y. Otani, and A. Barman, *Appl. Phys. Lett.* **104**, 072405 (2014).
- [34] V. P. Amin and M. D. Stiles, *Phys. Rev. B* **94**, 104420 (2016).
- [35] G. Y. Guo, Q. Niu, and N. Nagaosa, *Phys. Rev. B* **89**, 214406 (2014).
- [36] H. An, S. Haku, Y. Kageyama, A. Musha, Y. Tazaki, and K. Ando, *Adv. Funct. Mater.* **30**, 2002897 (2020).
- [37] S. Haku, A. Ishikawa, A. Musha, H. Nakayama, T. Yamamoto, and K. Ando, *Phys. Rev. Appl.* **13**, 044069 (2020).
- [38] W. Grange, M. Maret, J.-P. Kappler, J. Vogel, A. Fontaine, F. Petroff, G. Krill, A. Rogalev, J. Goulon, M. Finazzi, and N. B. Brookes, *Phys. Rev. B* **58**, 6298 (1998).
- [39] B. T. Thole, P. Carra, F. Sette, and G. van der Laan, *Phys. Rev. Lett.* **68**, 1943 (1992).
- [40] P. Carra, B. T. Thole, M. Altarelli, and X. Wang, *Phys. Rev. Lett.* **70**, 694 (1993).
- [41] T. Oguchi and T. Shishidou, *Phys. Rev. B* **70**, 024412 (2004).
- [42] J. Bartolomé, F. Bartolomé, L. M. García, E. Roduner, Y. Akdogan, F. Wilhelm, and A. Rogalev, *Phys. Rev. B* **80**, 014404 (2009).
- [43] P. Bruno, *Phys. Rev. B* **39**, 865 (1989).
- [44] B. F. Vermeulen, J. Wu, J. Swerts, S. Couet, D. Linten, I. P. Radu, K. Temst, G. Rampelberg, C. Detavernier, G. Groeseneken, and K. Martens, *J. Appl. Phys.* **120**, 163903 (2016).
- [45] F. Ibrahim, H. X. Yang, A. Hallal, B. Dieny, and M. Chshiev, *Phys. Rev. B* **93**, 014429 (2016).
- [46] K. Kita and A. Toriumi, *Appl. Phys. Lett.* **94**, 132902 (2009).
- [47] O. Krupin, G. Bihlmayer, K. Starke, S. Gorovikov, J. E. Prieto, K. Döbrich, S. Blügel, and G. Kaindl, *Phys. Rev. B* **71**, 201403(R) (2005).
- [48] A. Belabbes, G. Bihlmayer, S. Blügel, and A. Manchon, *Sci. Rep.* **6**, 24634 (2016).
- [49] Y. Kageyama, Y. Tazaki, H. An, T. Harumoto, T. Gao, J. Shi, and K. Ando, *Sci. Adv.* **5**, eaax4278 (2019).
- [50] S. E. Barnes, J. Ieda, and S. Maekawa, *Sci. Rep.* **4**, 4105 (2014).
- [51] R. H. Liu, W. L. Lim, and S. Urazhdin, *Phys. Rev. B* **89**, 220409(R) (2014).
- [52] H. An, T. Ohno, Y. Kanno, Y. Kageyama, Y. Monnai, H. Maki, J. Shi, and K. Ando, *Sci. Adv.* **4**, eaar2250 (2018).
- [53] T. Maruyama, Y. Shiota, T. Nozaki, K. Ohta, N. Toda, M. Mizuguchi, A. A. Tulapurkar, T. Shinjo, M. Shiraishi, S. Mizukami, Y. Ando, and Y. Suzuki, *Nat. Nanotechnol.* **4**, 158 (2009).
- [54] T. Koyama, Y. Nakatani, J. Ieda, and D. Chiba, *Sci. Adv.* **4**, eaav0265 (2018).